FUNCTIONAL MATERIALS
www.afm-journal.de

Advanced Photocatalysts: Pinning Single Atom Co-Catalysts on Titania Nanotubes

*Xin Zhou, Imgon Hwang, Ondřej Tomanec, Dominik Fehn, Anca Mazare, Radek Zboril, Karsten Meyer, and Patrik Schmuki**

Single atom (SA) catalysis, over the last 10 years, has become a forefront in heterogeneous catalysis, electrocatalysis, and most recently also in photocatalysis. Most crucial when engineering a SA catalyst/support system is the creation of defined anchoring points on the support surface to stabilize reactive SA sites. Here, a so far unexplored but evidently very effective approach to trap and stabilize SAs on a broadly used photocatalyst platform is introduced. In self-organized anodic TiO_2 nanotubes, a high degree of stress is incorporated in the amorphous oxide during nanotube growth. During crystallization (by thermal annealing), this leads to a high density of Ti^{3+}-O_v surface defects that are hardly present in other common titania nanostructures (as nanoparticles). These defects are highly effective for SA iridium trapping. Thus a SA-Ir photocatalyst with a higher photocatalytic activity than for any classic co-catalyst arrangement on the semiconductive substrate is obtained. Hence, a tool for SA trapping on titania-based back-contacted platforms is provided for wide application in electrochemistry and photoelectrochemistry. Moreover, it is shown that stably trapped SAs provide virtually all photocatalytic reactivity, with turnover frequencies in the order of 4×10^6 h^{-1} in spite of representing only a small fraction of the initially loaded SAs.

1. Introduction

Single atom (SA) catalysis, over the recent years, has become a highly investigated topic in heterogeneous catalysis.[1–6] In 2003, Fu and Flytzani-Stephnopoulos observed a water-gas-shift reaction, a very high catalytic activity when the precious metal catalyst was seemingly "completely leached out" of the catalyst support.[7] Nowadays, we know that this astonishing effect was due to a very low concentration of remaining finely dispersed Au or Pt atoms in a surface trapped $Me^{\delta+}$ state (i.e., mildly oxidized metal atoms in a surface coordinated position that were resistant to the cyanide leaching process employed for the removal of the metallic catalyst from the support).

In the meantime, supported SA catalysts have been explored for a wide range of "classic" heterogeneous catalysis reactions of high economic relevance, such as CO oxidation,[2,3,8–10] oxidation of alcohols, aldehydes, methane, or benzene,[11–15] for various hydrogenation reactions,[14,16,17] or in water-gas-shift and reforming reactions.[6,7,18–20]

Also in electrocatalysis, the high significance of SA catalysts has become clear,[21,22] including findings that point out entirely novel reaction pathways that become possible using SAs. For example, SA Pt catalysts were reported to provide selective electrochemical H_2O_2 production from O_2.[23]

In contrast to work that focuses on classic (thermal) catalysis or electrocatalysis, much less work has explored photocatalytic reactions where mobile charge carriers are generated in a semiconductor and then react with a red-ox species in the environment. In this type of charge transfer reaction, noble metals are very widely used as co-catalysts, for example, to promote the kinetics of slow reaction steps in photocatalytic H_2 generators, where the hydrogen evolution reaction (HER) needs to be catalyzed.[24–29]

X. Zhou, I. Hwang, Dr. A. Mazare, Prof. P. Schmuki
Department of Materials Science WW4-LKO
Friedrich Alexander University of Erlangen-Nuremberg
Martensstrasse 7, Erlangen 91058, Germany
E-mail: schmuki@ww.uni-erlangen.de

O. Tomanec, Prof. R. Zboril, Prof. P. Schmuki
Regional Centre of Advanced Technologies and Materials
Czech Advanced Technology and Research Institute
Palacký University Olomouc
Olomouc 77900, Czech Republic

The ORCID identification number(s) for the author(s) of this article can be found under https://doi.org/10.1002/adfm.202102843.

DOI: 10.1002/adfm.202102843

D. Fehn, Prof. K. Meyer
Department of Chemistry and Pharmacy
Inorganic Chemistry
Friedrich-Alexander University of Erlangen-Nuremberg
Egerlandstrasse 1, Erlangen 91058, Germany

Prof. R. Zboril
Nanotechnology Centre
Centre of Energy and Environmental Technologies
VŠB–Technical University of Ostrava
Ostrava 70800, Czech Republic

Prof. P. Schmuki
Department of Chemistry
Faculty of Science
King Abdulaziz University
P.O. Box 80203, Jeddah 21569, Saudi Arabia

Currently, mainly two semiconductors are frequently studied for SA mediated photocatalysis:[4] i) C_3N_4 (due to its visible light absorption and the relative stability of SAs as well as the ease of detection of SAs by aberration-corrected high-angle annular dark-field transmission electron microscopy (HAADF-TEM)); ii) anatase TiO_2 nanostructures (the classic benchmark photocatalyst with a wide range of applications and an outstanding photocorrosion stability).

In spite of remarkable achievements, a key challenge in all approaches to SA catalysis (dark or photo) is the control of trapping sites for SAs and the stability of these traps. Common fabrication methods for SA loaded substrates are either based on highly defined molecular-beam-soft-landing techniques or chemical trapping,[30–32] in combination with specific electronic or geometric trap features on substrates. Most effective trapping strategies involve encapsulation in zeolites, embedding in metal-oxide-frameworks, or insertion into molecular defects (as in C_3N_4). For classic inorganic semiconductors, most efforts to capture SAs rely on substrate defects such as lattice kinks, steps, or more effective on anion- or cation vacancies in surfaces in combination with adequate surface chemistries.[1,2,4,33,34] Establishing suitable trapping sites is not only the key to reactivity, but also perceived to be the main factor to provide SA stability against thermally induced agglomeration.

Recently, our group introduced a versatile approach to study SA trapping and photocatalytic reactions on single crystalline anatase flakes and thin-film layers of TiO_2.[35] The technique relied on a high-temperature reduction of TiO_2 to create defined Ti^{3+}-O_V states—these states then act as traps for Pt SAs; the trapping density can be controlled by the thermal reduction conditions applied to the substrate.

Here we introduce an entirely different, reduction-free approach that creates highly efficient SA trapping sites in a most widely used 3D structure for titania-based photocatalysis and photoelectrochemistry.[36,37]

2. Results and Discussion

In self-organized anodic TiO_2 nanotubes, such as in **Figure 1**a, during the growth of the amorphous oxide nanotube-structure, considerable strain is embedded in the tube walls.[38,39] This

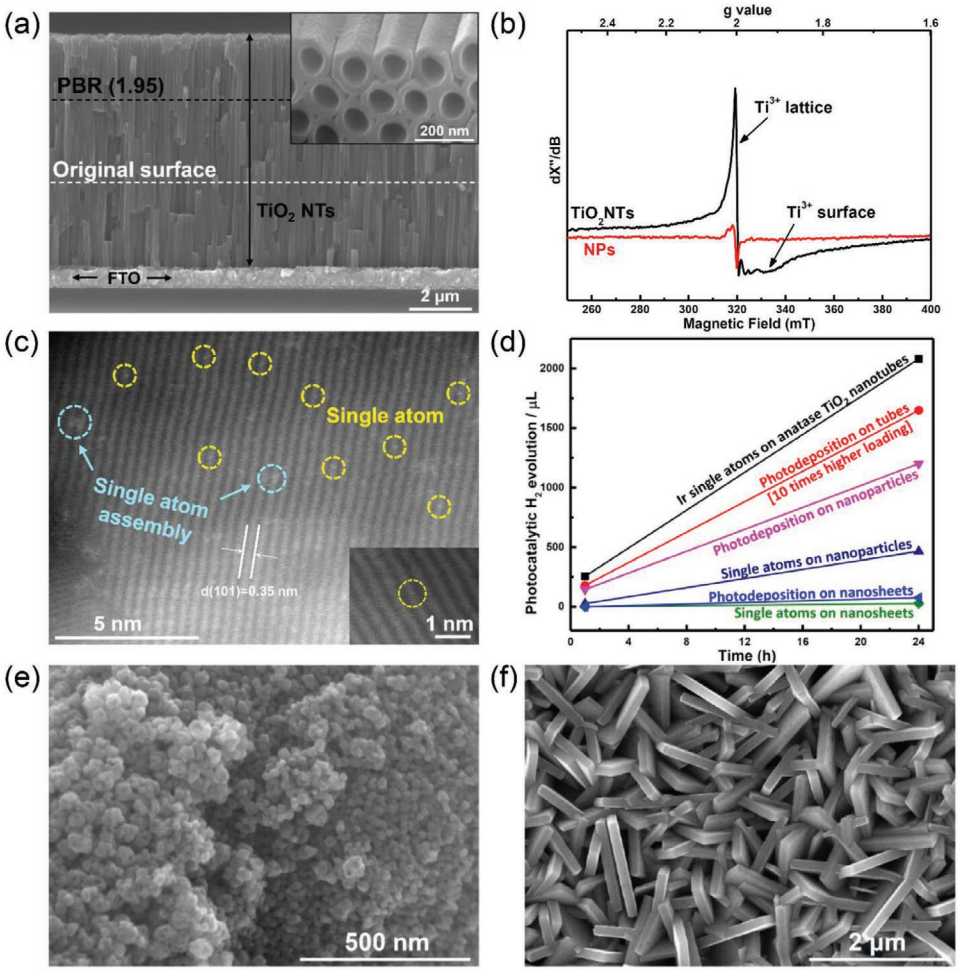

Figure 1. a) Cross-section SEM image of self-organized anodic TiO_2 nanotubes and an indication of expected length, Pilling-Bedworth ratio (PBR), and stress-induced elongation. The PBR of 1.95 and the original Ti layer are marked by dashed lines. The inset shows top-surface SEM image of TiO_2 nanotubes; b) EPR spectra of stress engineered TiO_2 nanotubes and anatase nanoparticles; c) HAADF-TEM images of Ir-SA-decorated TiO_2 nanotubes; d) Photocatalytic H_2 evolution of Ir decorated TiO_2 samples; SEM images of e) TiO_2 anatase nanoparticles and f) TiO_2 nanosheets.

is readily visible by an expansion of the tube length to values larger than what would be expected from the Pilling–Bedworth ratio (PBR),[40,41] as illustrated in Figure 1a. This expansion can be controlled by the anodic growth conditions of the tubes see Figures S1 and S2, Supporting Information). During thermal crystallization of these amorphous nanotubes, a high number of crystal defects is created,[42] and this defective structure is dependent on the growth conditions of the tubes as evident from electron paramagnetic resonance (EPR) (see Figure S3, Supporting Information). Figure 1b shows mass normalized EPR spectra for the nanotube layer grown to maximum expansion and annealed to anatase compared to commercial nanoparticulate (NP) anatase (see Figure S7a,b, Supporting Information, for further morphological specifications). Clearly, the nanotubes annealed to anatase show not only significantly stronger defect signals but importantly, also a distinctly different overall signature. While the NPs show one clear response at g = 2.0 corresponding to Ti^{3+} species in regular lattice positions,[43] the signature of the tubes shows an additional feature at $g_{avg} \approx 1.9$, which can be ascribed to surface-exposed Ti^{3+}-O_v states.[44] Evidently, this second type of defect is almost exclusively present in the nanotube samples and these defects, as we show below, are highly effective for SA trapping and the SA-Ir loaded tubes are highly active as an H_2 evolution co-catalyst.

It is noteworthy that depending on the growth conditions of the nanotubes (i.e., the water content in the electrolyte), not only significantly different expansion factors of the tubes can be obtained (Figure S2, Supporting Information) reflecting the embedded strain—as also indicated by Raman measurements (Figure S5, Supporting Information), but after annealing to anatase, the tubes provide a significantly different level of EPR active surface Ti^{3+}-O_V states (see Figure S3, Supporting Information) and in turn, this considerably affects the H_2 evolution rate of SA decorated nanotubes (Figure S4, Supporting Information).

Clearly, the tubes rich in surface-exposed Ti^{3+}-O_v states can be SA Ir decorated by immersing a nanotube sample in an $IrCl_3$ solution in the dark for 24 h (see methods section for details). Figure 1c shows a HAADF-STEM image of anodic TiO_2 NT layer grown to maximum expansion after crystallization to anatase and after Ir loading. After SA decoration, the tube structures show a photocatalytic H_2 evolution efficiency that clearly outperforms conventional decoration of the tubes with crystalline Ir nanoparticles produced by photodeposition (see Figure 1d)—this in spite of the much higher Ir loading achieved by photodeposition. Remarkably, if other TiO_2 nanostructures such as TiO_2 anatase nanoparticles or facetted nanosheet layers (see Figure 1e,f), either are SA loaded by immersion in $IrCl_3$ solution or are loaded by conventional photodeposition, they show a significantly lower photocatalytic H_2 performance than the SA decorated NTs (Figures S6 and S7, Supporting Information, show the corresponding scanning electron microscopy (SEM) morphologies of these reference structures). For all 3 morphologies after $IrCl_3$ immersion, no Ir nanoparticles can be detected by SEM, while after photodeposition on all nanostructures—as expected—Ir NPs of a typical size in the range of 2–10 nm are apparent. Most remarkable from the comparison of the different morphologies is that neither the significantly higher specific surface area of anatase nanoparticle, with Brunner–Emmett–Teller (BET) of ≈100 $m^2\ g^{-1}$ (vs BET≈30 $m^2\ g^{-1}$ for the nanotubes)[45] nor the presence of defined facets in single-crystalline sheets can reach the efficiency of the SA decorated nanotubes.

For these nanotubes, the uniformity of the SA trapping is evident from TEM-dispersive X-ray spectroscopy (EDX) in **Figure 2**a and further examples in Figure S8, Supporting Information. Over the entire tubes, no distinct Ir-particles can be detected (also detailed SEM investigations do not reveal any visible NPs, see Figure S6a, Supporting Information). The interaction of $IrCl_3$ with the surface defects at g_{avg}≈1.9 that are specific to the NTs, is apparent from the EPR spectra in Figure 2b. After interaction with $IrCl_3$, the nanotube sample shows a significant decrease in the magnitude of the signature at g_{avg}≈1.9. This strongly suggests that an attachment mechanism based on a galvanic displacement reaction, for example, $Ti^{3+} \rightarrow Ti^{4+}$; $Ir^{3+} \rightarrow Ir^{2+}{}_{surface\ trapped}$, takes place. This reaction eliminates EPR-active Ti^{3+} states and thus leads to a decrease in the magnitude of $g_{avg} \approx 1.9$.

Further details on the attachment chemistry can be obtained from X-ray photoelectron spectroscopy (XPS). XPS after surface trapping of Ir (24 h in the $IrCl_3$ solution) shows the presence of chloride (Cl 2p peak in Figure 2e)—this is in line with the TEM-EDX for chlorine in Figure 2a. An evaluation of the relative concentrations of iridium and chlorine from XPS yields 0.37 at.% Ir and 0.83 at.% Cl. This ratio of Ir:Cl of 1:2.2 means that the surface-attached Ir is still double coordinated with chloride. The high-resolution XPS peaks of Ir 4f (Figure 2c) and the Ir 4d (Figure 2d) are located at 61.86 (Ir 4f7/2) and 296.72 eV (Ir 4d5/2). The Ir 4f peak can be fitted in a contribution of iridium ($Ir^{\delta+}$) in a SA state (with the Ir 4f7/2 at 61.60 eV) and an overlapping Ti 3s signal at 61.90 eV. The XPS peak features for iridium in a SA state are well in line with a previous report on SA Ir in zeolite imidazolate frameworks.[46]

Ir cannot be detected by X-ray diffraction (XRD) (Figure S9, Supporting Information), but also SEM-EDX can provide direct information on the Ir loading of the different structures after immersion. Results on the iridium loading are summarized in Figure 2f and in **Table 1**. Evidently, immersion of the different titania morphologies leads to a similar Ir loading as determined from EDX. XPS generally gives a higher loading for photodeposited Ir, due to its surface sensitivity. The EDX results are in rough agreement with a more accurate determination of the integral Ir loading of the structures by powder analysis (using atomic absorption spectroscopy, AAS), where we obtain 0.58% for the nanotubes and 0.84% for the anatase nanoparticles, that is, the NTs and the NPs show a similar integral Ir loading in spite of a drastically different density of Ti^{3+}-O_V defect states. This indicates that only a minor fraction of Ir is trapped by galvanic displacement and as a consequence suggests that the drastically different photocatalytic reactivity of the two morphologies is due to a large difference in "truly" active sites. We propose that these highly active sites are the Ir SAs that are trapped by reaction with EPR active defects.

For all photodeposited samples, clearly, a 4–10 times higher loading is obtained than for the "dark" - immersion reaction (Table 1). Clearly, photodeposition leads to a much higher loading of the surface with crystallized Ir nanoparticles. If the Ir SA decorated nanotubes are subjected to illumination— that is, a photocatalytic experiment is performed—the surface composition and morphology change remarkably. First, after only 1 h

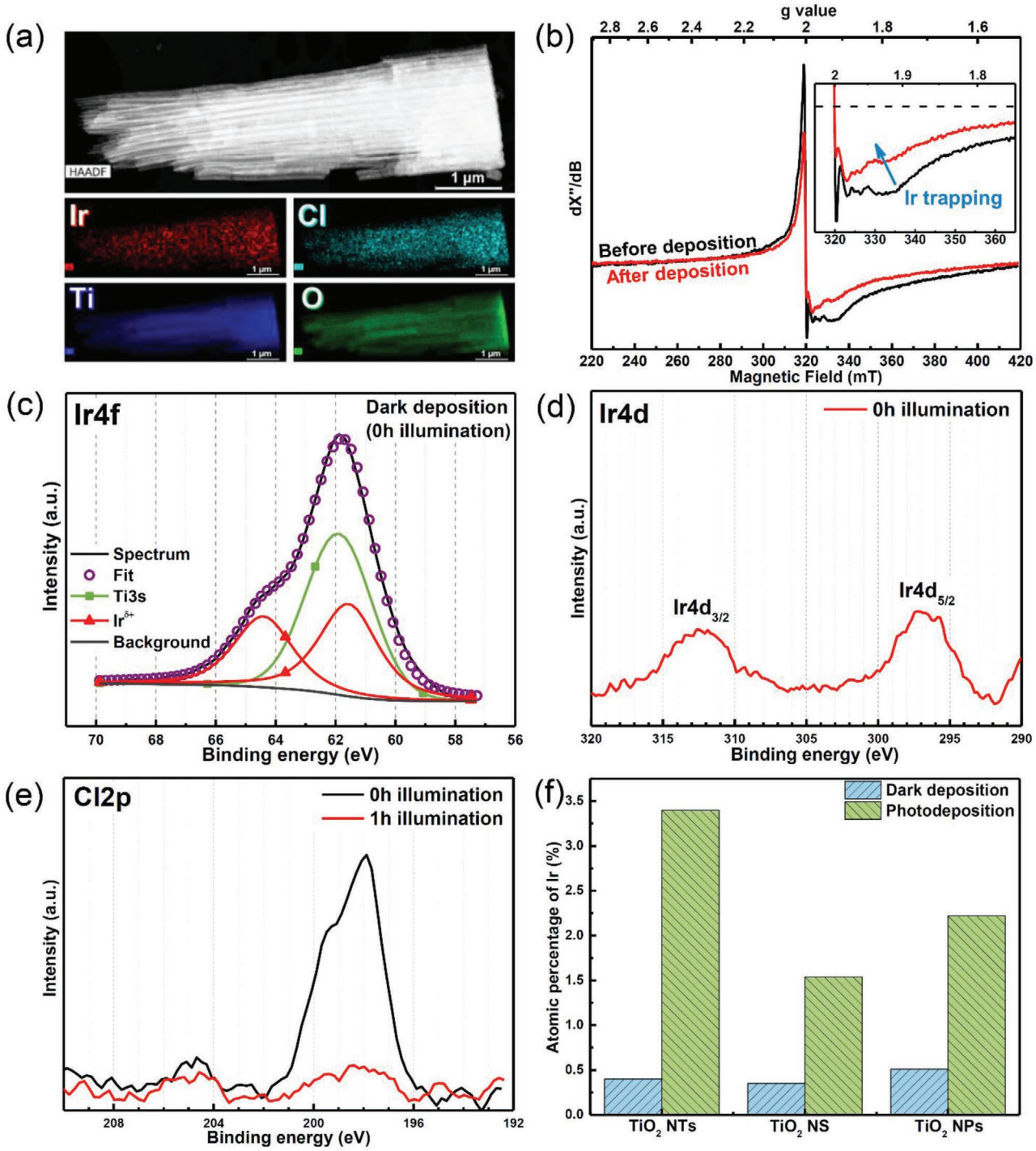

Figure 2. a) EDX element mapping of TiO_2 nanotubes immersed in $IrCl_3$ solution for 24h; b) EPR spectra of TiO_2 nanotubes before and after dark deposition of Ir SAs. (The inset shows the plots from ≈315–365 mT at higher magnification); high-resolution XPS spectra of c) Ir4f peak, d) Ir4d peak, and e) Cl2p peak after Ir dark deposition. Figure 2 (e) shows also the Cl2p peak after 1 h of illumination; f) Atomic percentage of Ir from EDX on dark deposited and photodeposited TiO_2 nanotubes, anatase nanoparticles, and nanosheets.

of illumination in the photocatalytic setting, the chlorine coordination of Ir is not detectable any more from XPS (Figure 2e) or from EDX (Figure S10, Supporting Information)—that is, illumination leads to a swift removal of the chloro-coordination of the surface trapped Ir. Also from the XPS Ir4f peak, significant changes occur over the photocatalytic reaction time (Figure S11d,e, Supporting Information). Already after 1 h of illumination, a conversion of the surface trapped $Ir^{\delta+}$ to metallic Ir^0 becomes apparent from the pronounced shoulder at lower binding energies, ≈60 eV. This is in line with SEM images taken after 1 h illumination (**Figure 3**a) where Ir nanoparticles with a size of ≈2 nm become visible (Figure 3b). With

Table 1. Atomic percentage of Ir from XPS and EDX of dark deposited TiO_2 nanotubes and anatase nanoparticles.

	Nanotubes, at% Ir		Nanoparticles, at% Ir	
	XPS	EDX	XPS	EDX
Dark deposition	0.37	0.40	2.37	0.51
Photodeposition	14.91	3.40	6.65	2.22

increasing illumination time, the number of SEM detectable Ir particles as well as their size increases (Figure 3a,b) and the surface composition extracted from XPS shows an increasing metallic Ir contribution. After 24 h illumination, 82% of the Ir is in a metallic state while the rest is mainly present as Ir^{4+}. However, a similar overall Ir concentration is maintained from the EDX (Figure S12, Supporting Information)—this confirms that a constant amount of Ir over illumination time is maintained (no loss to the solution occurs).

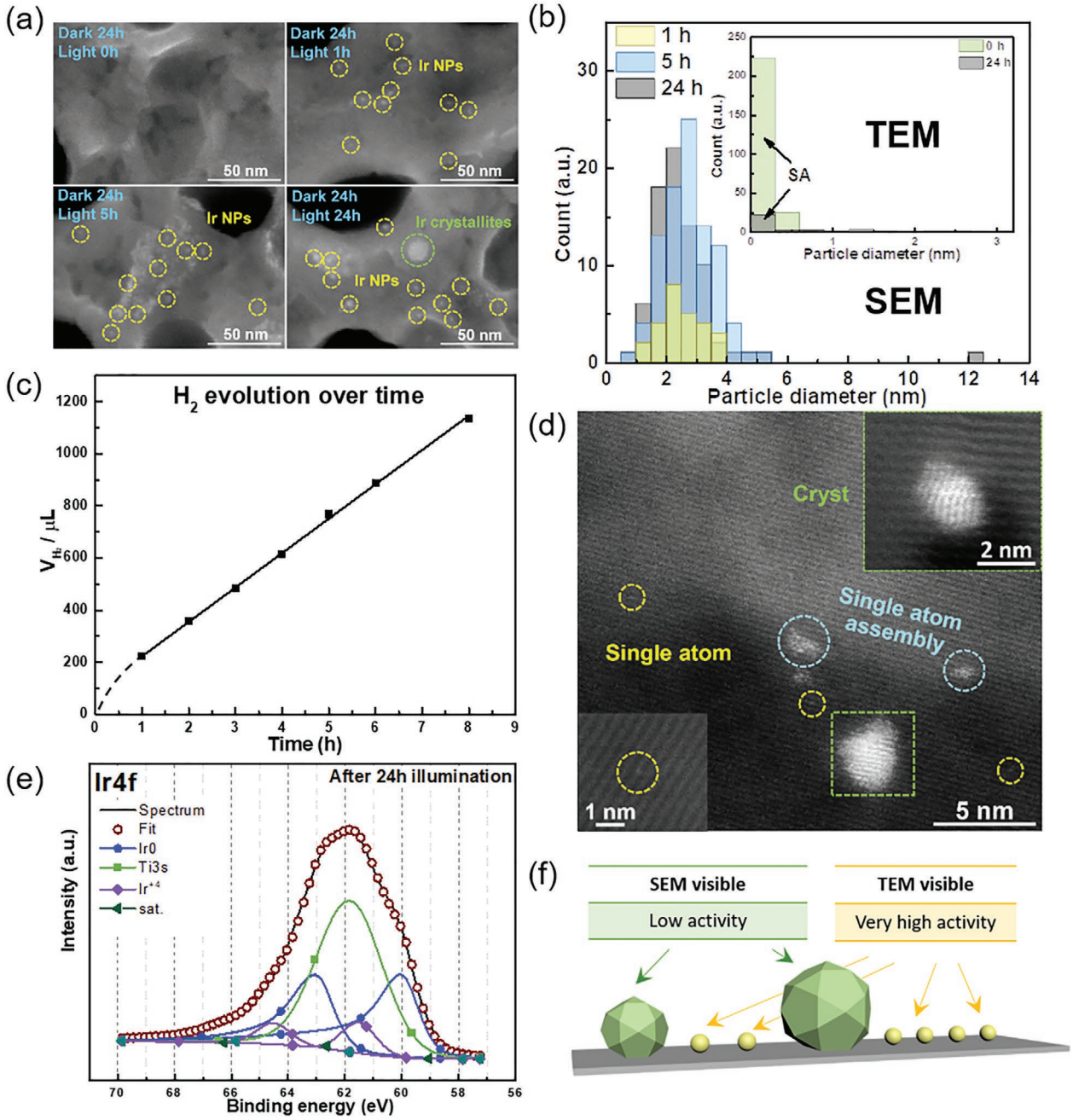

Figure 3. a) SEM images of Ir SA decorated TiO_2 nanotubes taken after different illumination times; b) Photoinduced particle agglomeration: Ir particle size distribution (from SEM, inset–from TEM) after different illumination times; c) Photocatalytic H_2 evolution over time for SA decorated TiO_2 nanotubes; d) HAADF-TEM images after 24 h illumination; e) Fitted Ir4f peak after SA decorated nanotubes were illuminated for 24 h; f) Schematic of the relationship between size and activity.

Over 24 h illumination, the TEM/SEM visible particle size increases from atomically defined features to aggregates and crystallites of an average size of 2.5 nm. This light-induced agglomeration is in stark contrast to the thermal stability of the SA configuration at room temperature (the TEM visible SA size distribution is virtually unchanged for samples stored for 6 months at room temperature). The HAADF-STEM taken after 24 h of illumination (Figure 3d) shows that indeed the vast majority of SAs have agglomerated into multimers (atomic dimers, trimers,....) or have even crystallized to nanoparticles (upper inset of Figure 3d)—also TEM-EDX directly confirms agglomeration (Figure S8, Supporting Information). The d-spacing of the crystallized particles in the inset of Figure 3d is 0.23 nm which corresponds well with the Ir (111) plane of metallic Ir.

More importantly, although a large amount of Ir has agglomerated into particles, the HAADF-TEM in Figure 3d shows that still SAs can be detected (see also the SEM images of 24h dark deposited and 24 illuminated nanostructures in Figure S13, Supporting Information, and the TEM-EDX mappings of Figure S14, Supporting Information). A comparison of the Ir SA density evaluated from HAADF-TEM before and after illumination yields 378'134 SAs per μm^2 before and 18'656 SAs per μm^2 after illumination.

Obviously, illumination has a crucial destabilization effect on most of the SAs attached to the surface which leads to their agglomeration to NPs. Nevertheless, in spite of this drastic agglomeration, almost no long-term drop in the photocatalytic H_2 activity is observed. In fact, Figure 3c shows that the photocatalytic H_2 production rate over illumination time does not drop significantly. For example: from SEM a strong agglomeration can be observed in the first 5 h of illumination, the rate (slope of the curve) does not drop (in the interval of 1–2 h the same amount of H_2 is generated as in the interval of 4–5 h). This means that in spite of agglomeration evident from SEM (please compare the distribution of particles in Figure 3b after 1 h and after 5 h), the reactivity of the entire photocatalyst is virtually maintained by a few truly active hot spots. After 24 h of illumination, we estimate approx. ≈18'000 Ir-SAs per μm^2 which corresponds to turnover frequency (TOF) of $\approx 4 \times 10^6$ h^{-1} while a classic assumption (that all Ir deposited on the structure is active) would results in a TOF of only 131.6 h^{-1} (for estimates see Figure S15, Supporting Information).

This finding supports the perception that in photocatalysis we often tend to ascribe "activity" to the wrong size of co-catalytic species. Specifically, in a large body of literature on photocatalysts, SEM investigations are used to characterize nanoparticles of co-catalysts and their size distribution to deduce connections to their activity. However, as in our case, the highest contribution to activity is provided by SEM invisible surface-linked SAs as summarized in Figure 3f.

3. Conclusion

In conclusion, our work introduces a novel anchoring architecture for SAs by exploiting intrinsic defects in anodically grown oxide nanostructures. In our case, we use Ir SAs trapped on anatase TiO_2 nanotube arrays to make an exceptionally active photocatalyst for H_2 evolution. The resulting trapped Ir SAs can provide a photocatalytic activity higher than SAs placed on other TiO_2 nanostructures (including nanostructures with a higher surface area or geometries that are facet-engineered). The photocatalytic activity is also higher than for conventional catalyst-NP decoration on TiO_2 nanostructures. We propose that the centers of reactivity are SAs trapped in the unique surface defects of anodic TiO_2 nanotubes—such SAs can reach TOFs of 4×10^6 h^{-1} and show high stability when anchored on this nanostructure.

4. Experimental Section

Materials: TiO_2 nanotubes were grown by anodizing on Ti foils (99.6%, 0.125 mm thick, Advent) in ethylene glycol-based (99.5%, Sigma-Aldrich) electrolyte containing 0.15 M NH_4F (98%, Sigma-Aldrich) and DI water (1, 3, or 5 wt. %). The Ti substrates were anodized at 60 V for 4.5C cm^{-2} at room temperature to reach 7 µm tube length. To convert the as-formed amorphous form of TiO_2 nanotubes to crystalline anatase, the samples were annealed in air at 450 °C for 1 h. In parallel, 3 µm thick Ti layers evaporated on FTO were used to evaluate the volume expansion factor for differently prepared TiO_2 nanotubes; the same anodization electrolyte and parameters were used for the Ti foil (see also Figure S1, Supporting Information).

Preferentially facetted (001) TiO_2 nanosheets were grown by a hydrothermal process on FTO substrates (7 Ω m^{-2}, Pilkington). For this, 1.5 mL titanium isopropoxide (Sigma-Aldrich) was dropped into aqueous hydrogen chloride (HCl) solution (30 mL DI water and 30 mL HCl (37%), Sigma-Aldrich) in a Teflon-lined stainless steel autoclave (capacity: 250 mL). After stirring for 15 min, 0.5 g ammonium hexafluorotitanate ($(NH_4)_2TiF_6$, Sigma-Aldrich) was added to the solution and stirring was continued for another 15 min. The hydrothermal synthesis was carried out at 150 °C for 15 h by immersing the pre-cleaned FTO (ultrasonication in acetone and ethanol, dried in a nitrogen stream) into the solution facing down. After rinsing with DI water, the as-formed nanosheets were annealed in air at 450 °C for 1 h to remove residual fluoride.

Anatase TiO_2 nanoparticles were purchased from Sigma-Aldrich (99.8%, ≈25–35 nm, BET ≈ 100 m^2 g^{-1}).

Ir Deposition on TiO_2 Samples: The iridium SA deposition, "dark deposition", on different TiO_2 structures was carried out in a quartz cell. The sample was immersed in 10 mL aqueous methanol solution (50 vol. %) containing 0.5 mM $IrCl_3$ ($IrCl_3 \cdot xH_2O$, Sigma-Aldrich). After 15 min purging with Ar to remove oxygen, the whole cell was kept in dark for 24 h. Moreover, the Ir dark deposited TiO_2 structures were immersed in ethanol for 15 min and in DI water for an additional 15 min, then the liquid was removed by drying in a nitrogen stream. A quartz cell containing 10 mL aqueous methanol solution (50 vol. %) was used for the hydrogen evolution measurements. After purging 15 min with Ar again, the sample was exposed to a LED (365 nm, 100 mW). The area of the illumination was approximately 1 cm^2. During the illumination, the solution was stirred with a magnetic stirrer at 1000 rpm and the hydrogen evolution was measured at 1 h, 2h, 3 h, etc., respectively. For anatase nanoparticles, 2 mg Ir loaded powder was dispersed in the same solution (same as for the nanotube layers) under magnetic stirring. Dark deposited powder was rinsed by centrifuging at 4000 rpm with 15 min in ethanol and 15 min in DI water. After drying in an oven, 2 mg powder could be collected and used for the hydrogen evolution measurement.

For the conventional photodeposition, the same process was used. Sample was immersed in 10 mL aqueous methanol solution (50 vol. %) containing 0.5 mM $IrCl_3$. After purging 15 min with Ar, the sample was immediately exposed to a LED (365 nm, 100 mW) for 24 h.

Characterization: The morphology and chemical composition of the samples were characterized by a field-emission scanning electron microscope (FE-SEM, Hitachi, S4800) and an Energy Dispersive X-Ray (EDAX Genesis, fitted to SEM chamber), respectively.

The composition and chemical state of samples were analyzed by XPS (PHI 5600). All XPS spectra were calibrated by shifting the spectra to a binding energy of Ti2p of 458.5 eV. Fitting of the peaks was performed

using Multipak software, using an asymmetric peak shape for the metallic iridium and a Gaussian-Lorentzian peak shape for the iridium deconvoluted peaks belonging to $Ir^{\delta+}$ or Ir^{4+} (the contribution from the $Ir5p_{1/2}$ and Ti3s peak were also considered; namely, the contribution of the $Ir5p_{1/2}$ peak in the Ir4f peak is small, estimated to be around 5% only,[47,48] and in addition, there is a contribution from the Ti3s peak at 61.9 eV—peak shape was determined from the bare TiO_2 nanotubes).

HAADF-TEM and EDS mapping of samples were carried out by a high-resolution transmission electron microscope (HRTEM, FEI Titan G2 60-300) and the crystalline structure of the samples was determined by X-ray diffraction analysis (XRD, X'pert Philips MPD, equipped with a Panalytical X'celerator detector) using graphite monochromized Cu Kα radiation, $\lambda = 1.54056$ Å.

The concentration level of the Ir loading on the nanotubes and on the nanoparticles were also determined by AAS with electrothermal atomization using a graphite furnace with a ContrAA 600 Spectrometer (Analytik Jena AG) equipped with a high-resolution Echelle double monochromator and with a continuum radiation source (Xe lamp).

Raman spectra were acquired for Raman shifts between 100 and 700 cm^{-1} using a Confocal Raman Microscope (LabRAM HR Evolution, Horiba, Dresden, Germany) with an excitation laser wavelength of 532 nm. The grating was set at 300 gr per mm.

The photocatalytic H_2 evolution was determined by a gas chromatograph (GCMS-QO2010SE, SHIMADZU) with a thermal conductivity detector (TCD).

EPR spectra of TiO_2 samples were recorded on a JEOL continuous wave spectrometer JES-FA200 equipped with an Xband Gunn oscillator bridge, a cylindric mode cavity, and a N_2 cryostat. The solid-state samples were measured in quartz EPR tubes under nitrogen atmosphere with a similar loading of ≈ 5 mg. All EPR spectra were measured with the following parameters: microwave frequency = 8.963 GHz, microwave power = 0.998 mW, modulation width = 1.0 mT, modulation frequency = 100 kHz, time constant = 0.1 s, and temperature = 95 K.

The TOF can be typically defined as:

$$\mathrm{TOF} = \frac{\mathrm{d}\mathrm{mol}(H)}{\mathrm{d}t} \times \frac{1}{\mathrm{mol}(A)} \quad (1)$$

where $\mathrm{d}\mathrm{mol}(H)/\mathrm{d}t$ represents the rate of hydrogen production per surface area, and $\mathrm{mol}(A)$ denotes the number of moles of active catalyst sites per surface area.[49] In the field of catalysis or particularly in photocatalysis, various approaches were considered for the evaluation of the number of active sites (for example see).[49] The most straightforward method in this case was determining the SA density directly from the HAADF-TEM images while also considering the reactive area to be represented by the illumination area (≈1 cm^2). As such, the TOFs were calculated by using the following equation:

$$\mathrm{TOF}(h^{-1}) = \frac{\text{number of evolved } H_2 \text{ molecules (per illuminated surface area)}}{\text{number of noble metal SA on } TiO_2 \text{ (per illuminated surface area)} \times \text{reaction time}} \quad (2)$$

Note that the above definition deviates from other methods used in photocatalysis.[49]

Supporting Information

Supporting Information is available from the Wiley Online Library or from the author.

Acknowledgements

The authors would like to acknowledge the DFG and the Operational research program, Development and Education (European Regional Development Fund, Project No. CZ.02.1.01/0.0/0.0/15_003/0000416 of the Ministry of Education, Youth and Sports of the Czech Republic) for financial support. Fahimeh Shahvaranfard is acknowledged for TiO_2 nanosheet preparation.

Open access funding enabled and organized by Projekt DEAL.

Conflict of Interest

The authors declare no conflict of interest.

Data Availability Statement

Research data are not shared.

Keywords

dark deposition, hydrogen generation, photocatalysis, single atom iridium, single-atom catalysis, TiO_2 nanotubes

Received: March 24, 2021
Published online: May 24, 2021

[1] J. Liu, *ACS Catal.* **2017**, *7*, 34.
[2] B. C. Gazes, M. Flytzani-Stephnopoulos, D. A. Dixon, A. Katz, *Catal. Sci. Technol.* **2017**, *7*, 4259.
[3] A. Wang, J. Li, T. Zhang, *Nat. Rev. Chem.* **2018**, *2*, 65.
[4] C. Gao, J. Low, R. Long, T. Kong, J. Zhu, Y. Xiong, *Chem. Rev.* **2020**, *120*, 12175.
[5] U. Heiz, A. Sanchez, S. Abbet, W. - D. Schneider, *J. Am. Chem. Soc.* **1999**, *121*, 3214.
[6] M. Flytzani-Stephanopoulos, *Acc. Chem. Res.* **2014**, *47*, 783.
[7] Q. Fu, H. Saltsburg, *Science* **2003**, *301*, 935.
[8] B. Qiao, A. Wang, X. Yang, L. F. Allard, Z. Jiang, Y. Cui, J. Liu, J. Li, T. Zhang, *Nat. Chem.* **2011**, *3*, 634.
[9] B. Qiao, J. -X. Liang, A. Wang, C. -Q. Xu, J. Li, T. Zhang, J. Liu, *Nano Res.* **2015**, *8*, 2913.
[10] B. Qiao, J. Liu, Y. -G. Wang, Q. Lin, X. Liu, A. Wang, J. Li, T. Zhang, J. Liu, *ACS Catal.* **2015**, *5*, 6249.
[11] Z. Huang, X. Gu, Q. Cao, P. Hu, J. Hao, J. Li, X. Tang, *Angew. Chem., Int. Ed.* **2012**, *51*, 4198.
[12] S. F. Hackett, R. M. Brydson, M. H. Gass, I. Harvey, A. D. Newman, K. Wilson, A. F. Lee, *Angew. Chem., Int. Ed.* **2007**, *46*, 8593.
[13] C. Zhang, F. Liu, Y. Zhai, H. Ariga, N. Yi, Y. Liu, K. Asakura, M. Flytzani-Stephanopoulos, H. He, *Angew. Chem., Int. Ed.* **2012**, *51*, 9628.
[14] W. Tang, Z. Hu, M. Wang, G. D. Stucky, H. Metiu, E. W. McFarland, *J. Catal.* **2010**, *273*, 125.
[15] D. Deng, X. Chen, L. Yu, X. Wu, Q. Liu, Y. Liu, H. Yang, H. Tian, Y. Hu, P. Du, R. Si, J. Wang, X. Cui, H. Li, J. Xiao, T. Xu, J. Deng, F. Yang, P. N. Duchesne, P. Zhang, J. Zhou, L. Sun, J. Li, X. Pan, X. Bao, *Sci. Adv.* **2015**, *1*, e1500462.
[16] B. Zugic, S. Zhang, D. C. Bell, F. Tao, M. J. Flytzani-Stephanopoulos, *J. Am. Chem. Soc.* **2014**, *136*, 3238.
[17] F. R. Lucci, J. Liu, M. D. Marcinkowski, M. Yang, L. F. Allard, M. Flytzani-Stephanopoulos, E. C. H. Sykes, *Nat. Commun.* **2015**, *6*, 8550.
[18] Y. Zhai, D. Pierre, R. Si, W. Deng, P. Ferrin, A. U. Nilekar, G. Peng, J. A. Herron, D. C. Bell, H. Saltsburg, M. Mavrikakis, M. Flytzani-Stephanopoulos, *Science* **2010**, *329*, 1633.

[19] X.-K. Gu, B. Qiao, C. -Q. Huang, W.-C. Ding, K. Sun, E. Zhan, T. Zhang, J. Liu, W.-X. Li, *ACS Catal.* **2014**, *4*, 3886.
[20] M. Yang, J. Liu, S. Lee, B. Zugic, J. Huang, L. F. Allard, M. Flytzani-Stephanopoulos, *J. Am. Chem. Soc.* **2015**, *137*, 3470.
[21] J. Kim, H. -E. Kim, H. Lee, *ChemSusChem* **2018**, *11*, 104.
[22] C. Zhu, S. Fu, Q. Shi, D. Du, Y. Lin, *Angew. Chem., Int. Ed.* **2017**, *56*, 13944.
[23] S. Siahrostami, A. Verdaguer-Casadevall, M. Karamad, D. Deiana, P. Malacrida, B. Wickman, M. Escudero-Escribano, E. A. Paoli, R. Frydendal, T. W. Hansen, I. Chorkendorff, I. E. L. Stephens, J. Rossmeisl, *Nat. Mater.* **2013**, *12*, 1137.
[24] G. Marcì, L. E. Palmisano, *Heterogeneous Photocatalysis: Relationships with Heterogeneous Catalysis and Perspectives*, Elsevier, Amsterdam **2019**.
[25] B. König, *Science of Synthesis: Photocatalysis in Organic Synthesis*, Thieme, Stuttgart **2019**.
[26] H. Kisch, *Semiconductor Photocatalysis: Principles and Applications*, Wiley-VCH, Weinheim **2014**.
[27] A. Fujishima, X. Zhang, D. A. Tryk, *Surf. Sci. Rep.* **2018**, *63*, 515.
[28] M. R. Hoffmann, S. T. Martin, W. Choi, D. W. Bahnemann, *Chem. Rev.* **1995**, *95*, 69.
[29] T. L. Thompson, J. T. Yates, *Chem. Rev.* **2006**, *106*, 4428.
[30] U. Heiz, A. Sanchez, S. Abbet, W. -D. Schneider, *J. Am. Chem. Soc.* **1999**, *121*, 3214.
[31] S. Vajda, M. G. White, *ACS Catal.* **2015**, *5*, 7152.
[32] R. E. Palmer, R. Cai, J. Vernieres, *Acc. Chem. Res.* **2018**, *51*, 2296.
[33] J. Jones, H. Xiong, A. T. DeLaRiva, E. J. Peterson, H. Pham, S. R. Challa, G. Qi, S. Oh, M. H. Wiebenga, X. I. P. Hernández, Y. Wang, A. K. Datye, *Science* **2016**, *353*, 150.
[34] J. A. Farmer, C. T. Campbell, *Science* **2010**, *329*, 933.
[35] S. Hejazi, S. Mohajernia, B. Osuagwu, G. Zoppellaro, P. Andryskova, O. Tomanec, S. Kment, R. Zbořil, P. Schmuki, *Adv. Mater.* **2020**, *32*, 1908505.
[36] K. Lee, A. Mazare, P. Schmuki, *Chem. Rev.* **2014**, *114*, 9385.
[37] I. Paramasivam, H. Jha, N. Liu, P. Schmuki, *Small* **2012**, *8*, 3073.
[38] P. Skeldon, G. E. Thompson, S. J. Garcia-Vergara, L. Iglesias-Rubianes, C. E. Blanco-Pinzon, *Electrochem. Solid-State Lett.* **2006**, *9*, B47.
[39] K. Hebert, S. Albu, I. Paramasivam, P. Schmuki, *Nat. Mater.* **2012**, *11*, 162.
[40] S. P. Albu, P. Schmuki, *Electrochim. Acta* **2013**, *91*, 90.
[41] S. Berger, J. M. Macak, J. Kunze, P. Schmuki, *Electrochem. Solid-State Lett.* **2008**, *11*, C37.
[42] S. So, P. Schmuki, *Angew. Chem., Int. Ed.* **2013**, *52*, 7933.
[43] N. Liu, C. Schneider, D. Freitag, M. Hartmann, U. Venkatesan, J. Müller, E. Spiecker, P. Schmuki, *Nano Lett.* **2014**, *14*, 3309.
[44] A. Naldoni, M. Altomare, G. Zoppellaro, N. Liu, Š. Kment, R. Zbořil, P. Schmuki, *ACS Catal.* **2019**, *9*, 345.
[45] S. Mohajernia, P. Andryskova, G. Zoppellaro, S. Hejazi, S. Kment, R. Zboril, J. Schmidt, P. Schmuki, *J. Mater. Chem. A* **2020**, *8*, 1432.
[46] M. Xiao, J. Zhu, G. Li, N. Li, S. Li, Z. P. Cano, L. Ma, P. Cui, P. Xu, G. Jiang, H. Jin, S. Wang, T. Wu, J. Lu, A. Yu, D. Su, Z. Chen, *Angew. Chem., Int. Ed.* **2019**, *58*, 9640.
[47] V. Pfeifer, T. E. Jones, J. J. V. Vélez, C. Massué, R. Arrigo, D. Teschner, F. Girgsdies, M. Scherzer, M. T. Greiner, J. Allan, M. Hashagen, G. Weinberg, S. Piccinin, M. Hävecker, A. Knop-Gericke, R. Schlögl, *Surf. Interface Anal.* **2016**, *48*, 261.
[48] S. Freakley, J. Esquius, D. Morgan, *Surf. Interface Anal.* **2017**, *49*, 794.
[49] N. Serpone, A. Salinaro, A. Emeline, V. Ryabchuk, *J. Photochem. Photobiol., A* **2000**, *130*, 83.